



Damage localization in carbon fiber composite plate combining ultrasonic guided wave instantaneous energy characteristics and probabilistic imaging method

Feiyu Teng^a, Juntao Wei^a, Shanshan Lv^a, Xiangyi Geng^a, Chang Peng^b, Lei Zhang^a, Zengye Ju^b, Lei Jia^a, Mingshun Jiang^{a,*}

^a School of Control Science and Engineering, Shandong University, Jinan 250000, China

^b CRRC Qingdao Sifang Co. Ltd, Qingdao, 266111, Shandong, China

ARTICLE INFO

Keywords:

Carbon fiber composite plate
HHT
Ultrasonic guided wave
Damage localization
Probability imaging method

ABSTRACT

The ultrasonic guided wave (UGW) imaging technique has become a promising tool in composite structure health monitoring. However, most algorithms extract damage characteristics with time or frequency domain method. These methods cannot characterize the nonlinear and nonstationary damage signals. Based on the Hilbert–Huang transform, the phenomenon of instantaneous energy increase and decrease is studied, and the rule of energy change and distance from damage to sensor path is summarized. The damage index based on instantaneous energy characteristics is proposed. A probabilistic imaging method is proposed, which introduces a probability distribution function based on the elliptical method for fusion imaging with traditional probability distribution function. The experiment of 74 points on carbon fiber composite plate was performed. The average localization error was 3.56 mm and the maximum was 9.68 mm. The proposed method has high localization accuracy and stability and has application prospects in high-end equipment composite structure health monitoring.

1. Introduction

In recent years, due to the excellent material properties including light weight, high specific strength, high temperature resistance, corrosion resistance, and strong design ability [1–5], carbon fiber composite materials have been widely used in the aircraft body, high-speed train, subway body, and bogie [6,7]. The weight ratio of carbon fiber composite materials used has become one of the important indicators of the advanced degree of high-end equipment. However, carbon fiber composite structures may appear defects during the complex manufacturing process, delamination and fatigue cracks may occur during long-term service resulting from external impact or fatigue loading, causing performance degradation and threatening operational safety. Therefore, it is of great significance to study structural health monitoring and damage detection techniques of composite structures [8–10].

Ultrasonic guided wave (UGW) is an elastic wave with a long propagation distance, small amplitude loss, and high damage sensitivity. UGW technology, which takes damage information as transmission medium, has high sensitivity and monitoring efficiency. It has become a research hotspot in the field of nondestructive testing [11–15].

Characterization of damage with response signals has always been an important research element in UGW technology. After the sensor acquires the response signal, using analysis algorithms to extract the carried damage characteristics is the key step to achieve structure damage detection and state monitoring. However, it is hard to analyze the UGW because of its multimode and dispersion characteristics. Presently, signal analysis algorithms can be divided into the time domain, frequency domain, and time-frequency domain analysis. The commonly time domain analysis include correlation [16–18], time-of-flight (TOF) [19] and amplitude [20]. Correlation and amplitude analysis methods have a simple and fast processing process but contain less information which makes it difficult to accurately determine the health status of the structure. TOF relies on wave velocity which is difficult to apply in composite materials. The frequency domain analysis uses Fourier transform, which has the advantages of anti-interference and correlation between characteristic change and frequency. But the Fourier analysis has strict restrictions on its use, the system analyzed must be linear and the signal must be strictly periodic and stable [21,22]. However, most of the signals generated by the interaction of UGW with damage in carbon fiber composites

* Corresponding author.

E-mail address: jiangmingshun@sdu.edu.cn (M. Jiang).

are nonlinear and nonstationary. The signal analysis method based on the Fourier transform cannot effectively extract these damage features. In the time-frequency domain, the short-time Fourier transform and wavelet transform depend on the choice of the time window and wavelet basis, the adaptability is poor [23,24]. Therefore, as an adaptive signal analysis algorithm suitable for analyzing nonlinear and nonstationary signals, the Hilbert-Huang transform (HHT) is introduced to characterize the damage characteristics of acoustic signals.

HHT, a time-frequency signal processing method proposed by Norden E. Huang in 1998 [25], is considered a major breakthrough in the field of Fourier transform-based linear and steady-state spectral analysis. Currently, HHT is prominent in applications of acoustic signal-based structure damage detection such as mechanical loosening vibration signals [26], bearing damage vibration signals [27], and acoustic emission signals [28]. Li Lin [29] compared the effects of HHT, Fourier transform and wavelet transform on fatigue damage acoustic signal and found that HHT had a more sensitive time-frequency resolution and more precise energy definition. Baochun Xu [30] introduced the HHT method to UGW-based structure health monitoring. In their study, the marginal spectrum was obtained by HHT and compared with the spectrum. It was shown that the marginal spectrum could better represent the signal variation. In [31], they studied the description method of damage information in the signal in terms of both instantaneous phase and marginal spectrum distribution. This work demonstrated that the instantaneous features extracted from the marginal spectrum could describe the damage better, but did not perform damage localization and imaging. Chenhui Su [32] used HHT to obtain the energy-frequency spectrum to calculate the damage factor and used the tomography algorithm to perform single-damage and multi-damage localization in a carbon fiber composite plate.

In this paper, a probabilistic imaging damage localization method based on UGW instantaneous energy characteristics is proposed. Compared with the previously mentioned work, this paper focuses on the damage characterization ability of the signal instantaneous energy characteristics and the relationship between the energy characteristics variation and the damage location. In previous research, signal energy variation is an effective method for damage information characterization [33,34]. The HHT method has a finer energy definition and a special performance form. Therefore, it is worth studying the various rules of signal instantaneous energy characteristics before and after damage and the application methods for localization. Some papers have carried out preliminary research on this; for example, Bingquan Wang [35] studied the instantaneous energy characteristics and probabilistic imaging methods and performed area estimation of the damage. However, the air-coupled devices used limit the discussion of the relationship between damage location and instantaneous energy characteristics in this study, also, there is not to clarify the relationship between energy characteristic values and damage. In addition, the signal and application method of this device is quite different from the permanent piezoelectric lead zirconate titanate (PZT) array detection method. In order to meet the demand of structural health monitoring, the signal acquired by the PZT array should still be the research object. In this paper, experiments were performed using a PZT sensor array arranged on a carbon fiber composite to study the relationship between the signal instantaneous energy characteristic variation and the damage location. The proposed method uses the damage index based on the instantaneous energy to characterize the damage information and designs a valid path screening method using the increase and decrease of energy. The probabilistic imaging algorithm is used to calculate the location of simulated damage on the carbon fiber composite plate. The experiment results prove the effectiveness of the proposed method. This method improves the time-frequency resolution, reduces the influence of the human intervention on the results, and the localization accuracy is greatly improved.

The remaining chapters of the paper are arranged as follows. Section 2 introduces the HHT signal processing process and the probabilistic imaging algorithm. Section 3 shows the setup of the experimental

system, analyzes the relationship between the instantaneous energy characteristic variation and the damage location and performs numerical simulation to verify the principle of the phenomenon. Section 4 proposes modified damage indexes and improved probabilistic imaging method, and discusses the localization results. Finally, conclusions are drawn in Section 5.

2. HHT signal processing methods and probabilistic imaging algorithm

2.1. HHT signal processing

The UGW propagating in the carbon fiber composite plate has more complex dispersion characteristics, and the waves with damage information are mostly nonlinear and nonstationary. Therefore, HHT is proposed to analyze the signal, and the instantaneous energy is obtained as a characteristic parameter for damage analysis. The HHT method consists of empirical modal decomposition (EMD) and Hilbert transform. The first step performs EMD on the signal, which adaptively decomposes the signal into a series of intrinsic mode functions (IMFs) according to the signal features, each of which is independent and meets two conditions at the same time: (1) the number of extreme points and the number of zeros are equal or the difference is 1; (2) The local average of the upper envelope defined by the maximum and the lower envelope defined by the minimum is 0. The second step performs the Hilbert transform on the extracted IMFs that the signal is analyzed in the time-frequency domain. The signal processing process is given below.

The signal $f(t)$ acquired from the sensor is assumed to be decomposed into k IMFs, and the k th IMF is denoted as $c_k(t)$. The upper and lower envelopes are generated by first fitting the local maximum points and minimum points by the cubic spline function. Their mean value is denoted as $m(t)$ and $h(t)$ is obtained by subtracting this mean sequence from the original signal. If $h(t)$ does not meet the two conditions mentioned previously, take it as the new original signal and repeat the above steps until the conditions are met. Here the first IMF is obtained: $c_1(t) = h(t)$, the residual signal $r(t) = f(t) - c_1(t)$, which will be considered as the new input signal. Repeat the above process to obtain the remaining IMFs. When $r(t)$ meets a monotonic sequence or constant value sequence, the full IMF extraction process is completed, and the final $r(t)$ is called the residual term. The decomposition process of the signal can be expressed as:

$$f(t) = \sum_{i=1}^k c_i(t) + r(t). \quad (1)$$

After the all IMFs are obtained, the Hilbert transform is performed on every IMF to obtain the unique Hilbert spectrum $H_i(t, f_i)$ of each IMF. Huang defines the Hilbert spectrum of all IMFs as $H(t, f)$. It is a three-dimensional diagram consisting of the time, instantaneous frequency, and instantaneous amplitude of all IMFs. The distribution of the signal energy in the time-frequency domain can be obtained from this diagram. The instantaneous energy, as in Eq. (2), is used to represent the variation of signal energy with time.

$$IE(t) = \int_f H^2(t, f) df \quad (2)$$

2.2. Probabilistic imaging algorithm

The core concept of the probabilistic imaging algorithm is based on the physical principle that damage on the direct path can produce the most significant change in the GW and the amplitude of the change decreases as the distance between the damage and the direct wave path increases. When the distance is exceeded a certain range, there will be no change in the response signal acquired for a limited length of time. It is necessary to obtain the baseline signal from the intact structure

Table 1
The specific parameters of PZT sensor.

Parameter		Value	Parameter		Value
Dimension (mm)	Thickness	0.48	Relative permittivity	ϵ_{11}	1700
	Diameter	8		ϵ_{33}	1700
Density (10^3 kg/m ³)		7.7	Mechanical quality factor	Q_m	150
Compliance coefficient ($\times 10^{-12}$ m ² /N)	s_{11}	15	Piezoelectric constant ($\times 10^{-12}$ C/N)	d_{31}	160
	s_{33}	9		d_{33}	400
	s_{55}	25		d_{15}	480

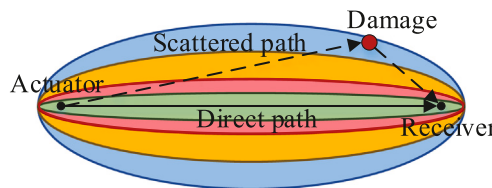


Fig. 1. Probabilistic imaging principle.

in advance and compare it with the detection signal obtained during the detection process. The formula consists of damage index (DI) and probability distribution function, where DI is the quantization of the signal change and the probability distribution function represents the position relationship between the pixel point and the sensor path.

It is assumed that a sensor network consists of N sensor paths, and discretizing the area inside the network, the probability of damage existing at the point (x, y) is expressed as:

$$P(x, y) = \sum_{k=1}^N p_k(x, y) = \sum_{k=1}^N DI_k \cdot TW_k[R_k(x, y)], \quad (3)$$

where $p_k(x, y)$ is the probability that the signal change of the k th sensor path is affected by (x, y) , DI_k and $TW_k[R_k(x, y)]$ is its DI and traditional probability distribution function, respectively. When DI is larger, the signal variation is more significant, and when DI is smaller, the signal variation is less. If the baseline signal and detection signal are identical, the value of DI is 0. The traditional probability distribution function is a set of elliptical contours with the same focus and different widths, which linearly decreases between 1 and 0. It provides a weight value for DI. The closer the pixel point is to the sensor path, the larger the weight value is, and vice versa, the smaller the weight value is. The weight value is 0 after exceeding the detection range. The distribution of weights is shown in Fig. 1, and the function is expressed as:

$$TW_k[R_k(x, y)] = \begin{cases} 1 - \frac{R_k(x, y)}{\beta}, & R_k(x, y) < \beta \\ 0, & R_k(x, y) \geq \beta \end{cases}, \quad (4)$$

where β is the shape factor dominating the elliptical detection range and $R_k(x, y)$ is defined as the relative distance from the (x, y) to the k th sensor path, calculated by:

$$\begin{aligned} R_k(x, y) &= \frac{D_{ak}(x, y) + D_{sk}(x, y)}{D_k(x, y)} - 1 \\ &= \frac{\sqrt{(x - x_{ak})^2 + (y - y_{ak})^2} + \sqrt{(x - x_{sk})^2 + (y - y_{sk})^2}}{\sqrt{(x_{ak} - x_{sk})^2 + (y_{ak} - y_{sk})^2}} - 1, \end{aligned} \quad (5)$$

where (x_{ak}, y_{ak}) and (x_{sk}, y_{sk}) are actuator and receiver coordinates of the k th sensor path, $D_{ak}(x, y)$ and $D_{sk}(x, y)$ represent the distance from (x, y) to them, respectively, $D_k(x, y)$ is this path distance.

The difference between the instantaneous energy of the baseline signal and the detection signal is defined as the damage index. Two DIs based on instantaneous energy are defined, the energy value damage index (EVDI) and the energy ratio damage index (ERDI):

$$EVDI = \int \left| \widetilde{IE}_x(t) - \widetilde{IE}_y(t) \right| dt, \quad (6)$$

Table 2
Coordinates of PZT sensors pasted on the plate.

Sensor	Coordinate (mm)	Sensor	Coordinate (mm)	Sensor	Coordinate (mm)
S1	(-100, 0)	S5	(50, 86.6)	S9	(50, -86.6)
S2	(-86.6, 50)	S6	(86.6, 50)	S10	(0, -100)
S3	(-50, 86.6)	S7	(100, 0)	S11	(-50, -86.6)
S4	(0, 100)	S8	(86.6, -50)	S12	(-86.6, -50)

$$ERDI = \int \left| \frac{IE_x(t) - IE_y(t)}{IE_x(t)} \right| dt, \quad (7)$$

where, $IE_x(t)$ and $IE_y(t)$ are the instantaneous energy of the baseline signal and the detection signal. For EVDI, the structure and path length will cause large differences in the instantaneous energy amplitudes of signals from different paths. In order to make comparisons under the same criterion, a normalization process (superscript \sim) is performed, and the standard value is the maximum of the absolute values of the two energy numerical sequences.

3. Study on instantaneous energy characteristics of UGW

3.1. Experiment system introduction

The experimental system was constructed as shown in Fig. 2, including a carbon fiber composite plate, PZT sensor array, ultrasonic guided wave detector, and upper computer. The size of The T700 carbon fiber composite plate is 450 mm × 450 mm × 2.4 mm, fiber laying is [0/90]_{3s}. The sensor array is a circular array consisting of 12 PZT sensors and the effective detection area of 200 mm diameter inside. The detail parameters of PZT can be seen in Table 1. The pitch-catch mode is used, and since the actuator and receiver sensors do not influence the received signal when they are swapped, the detection job is set only once for the actuator Si-receiver Sj sensor pair, and the sensor path is defined as P_{i-j} . The sensor network consists of 66 sensor paths, the numbers from 1 to 66 correspond to the names from P_{1-2} to P_{11-12} , respectively. A rectangular coordinate system is established with the circle center of the detection area as the origin point. The sensor coordinates and network are shown in Table 2 and Fig. 2(b), respectively.

The ultrasonic guided wave detector has signal generation, power amplification, channel switching, and high-speed data acquisition functions. The amplitude of excitation signal is set to ±80 V and the sampling frequency is set to 10 MHz. The upper computer controls the detector to perform detection tasks and damage analysis.

3.2. Excitation frequency selection

Due to the anisotropy of composite materials, the propagation velocities of UGW with the same frequency and same mode are different in different directions. Fig. 3 shows the dispersion curves of the experimental plate (specific parameters are shown in Table 3), which were calculated by software named Dispersion Calculator v2.1 designed by German Aerospace Center. It can be seen that there are at least two modes in the structure, and when the frequency is less than 300 kHz,

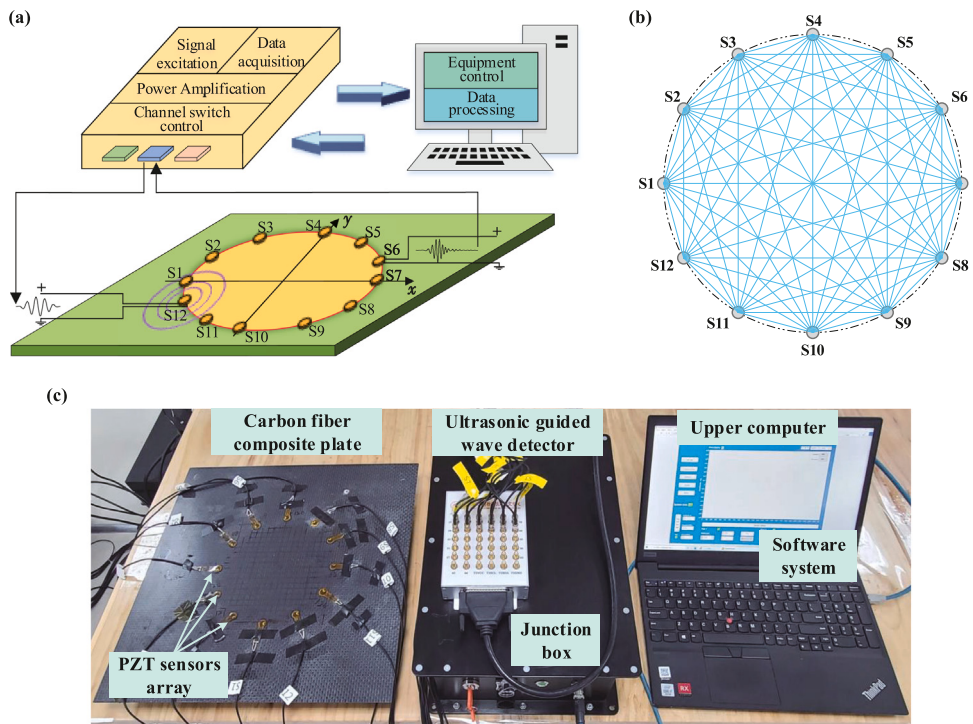


Fig. 2. Experimental system set up (a) schematic diagram; (b) sensor network; (c) experimental diagram.

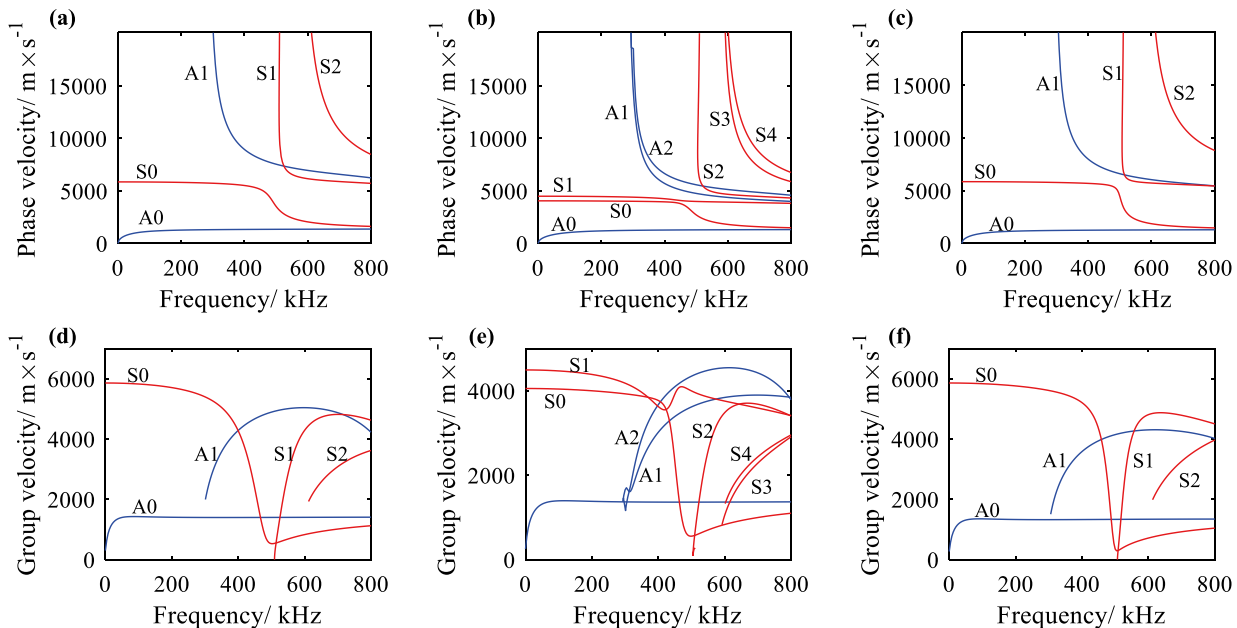


Fig. 3. Dispersion curves of carbon fiber composite plate (a) (b) and (c) are the phase velocity of 0°, 45°, 90°; (d) (e) and (f) are the group velocity of 0°, 45°, 90°.

Table 3
Material properties of the carbon fiber composite plate used in this paper.

Young's modulus (GPa)			Shear modulus (MPa)			Poisson's ratio			Density (kg m ⁻³)
E ₁	E ₂	E ₃	G ₁₂	G ₁₃	v ₂₃	v ₁₂	v ₁₃	v ₂₃	ρ
114	8.61	8.61	4160	4160	3000	0.3	0.3	0.45	1800

mainly A0 and S0 modes exist in the structure. When the excitation signal is selected, the lesser modes present in the structure will help simplify the difficulty of signal analysis and improve accuracy.

As for a determined structure, the frequency of the excitation signal decides the UGW modes generated in the structure and the basic parameters such as amplitude and wave speed of each mode. Therefore, it is important to select a suitable frequency so that the UGW in the structure includes a main mode with large amplitude and is easily distinguishable compared to other modes. Due to the slower phase velocity, shorter wavelength, and higher damage sensitivity, the A0

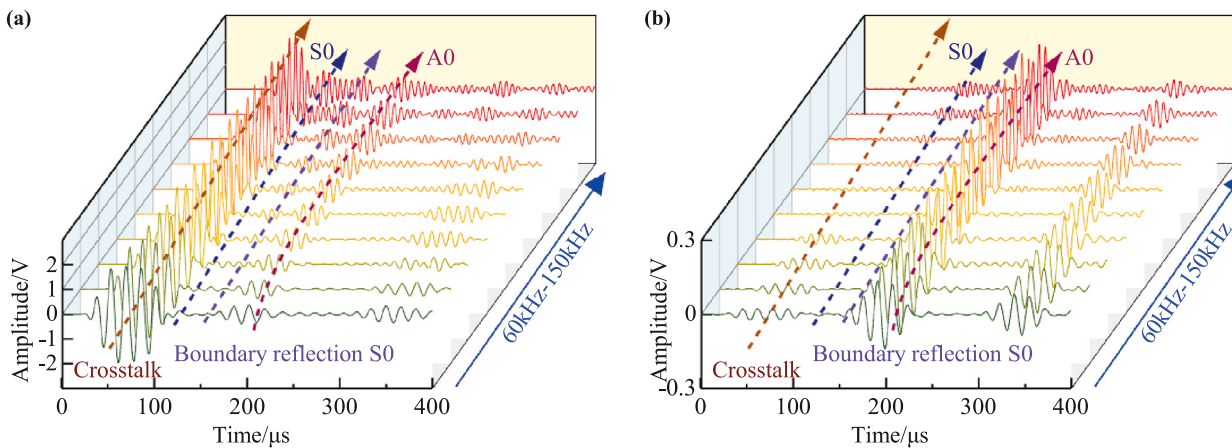


Fig. 4. UGW signals of sensor path P_{1-7} with different excitation frequencies (a) baseline signals; (b) scattered signals.

mode has been selected more over the other fundamental mode. Research shows that in carbon fiber composite plate, the UGW generated by low frequency excitation is dominated by A0 mode. The Hanning-windowed 5 cycles sinusoidal tone burst is the excitation signal, which center frequency in steps of 10 kHz between 60 kHz and 150 kHz, respectively. Fig. 4(a) shows the signals of sensor path P_{1-7} with the intact structure. As shown in Fig. 4(a), in 60 kHz–150 kHz, the UGW includes two modes, A0 and S0. When the center frequency is 60 kHz, A0 is dominant and S0 is basically invisible. In 60 kHz–130 kHz, the amplitude of S0 mode increases with the increase of frequency and is equal to A0 at 130 kHz. When the damage is at (0, 0), the signal is excited from 60 kHz to 150 kHz and the detected signals are obtained. Fig. 4(b) shows the scattered signals of P_{1-7} , obtained by subtracting the detected signal from the baseline signal. The scattered signal can represent the signal change that occurs by the damage. It can be seen that the damage mainly affects the A0 mode at these frequencies. At 130 kHz–150 kHz, the scattered signal of the S0 mode starts to be visible gradually. Considering the three factors of mode aliasing, amplitude, and mode mainly affected by damage, 110 kHz is selected as the center frequency, and A0 mode will be analyzed and processed later. In order to obtain a cleaner signal and reduce unnecessary IMF components, the acquired signal is filtered by an 80 kHz–140 kHz bandpass filter. Because the excitation signal is a modeled narrow-band signal, the bandpass filter can eliminate abnormal intermittent signals (such as high-frequency noise) in the acquired signal while retaining the effective signal, and suppressing the modal mixing phenomenon of EMD decomposition.

损伤尺寸 The ability of damage detection by UGW is related to the selected mode wavelength. In general, it is detectable when the damage size is more than half of the wavelength. Since the phase velocities of the composite materials are different in each direction, the average velocity of them is used to obtain the wavelength of the current A0 mode as 11.05 mm. Therefore, in this experimental setup, the size of the applied damage is to be larger than 5.025 mm.

3.3. Test points setup

损伤模拟 The damping clay was selected to simulate the damage due to its mechanical properties, which cause both attenuation and phase shifting on the UGW. Due to the laying sequence of the plate, the sensor network is arranged in the center of the plate. Therefore the test results in a single quadrant can represent the detection effect of the complete detection area. In the fourth quadrant, 74 test points were selected for damage localization experiments. The shape of the clay is about 10 mm diameter circle which satisfy detectable conditions greater than half the wavelength. The distribution of test points is shown in Fig. 5, with a coordinate step of 10 mm.

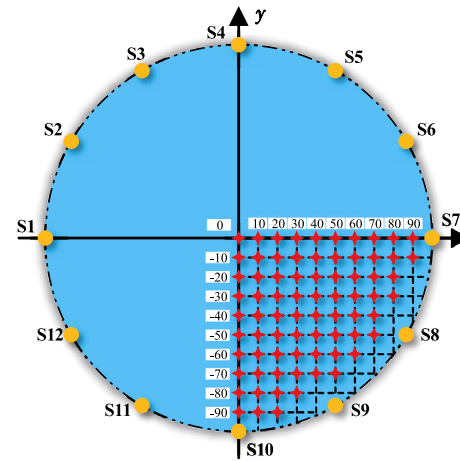


Fig. 5. Test points in the coordinate system.

3.4. Analysis of the instantaneous energy of the UGW

The experimental data of the test point (0, 0) is analyzed as an example. The signal processing process for the sensor path P_{1-8} is shown in Fig. 6. The baseline signal and the detected signal are the response signals acquired before and after the application of the simulated damage, respectively. Due to the damage, the direct wave of the detected signal is different from the baseline signal. The EMD decomposition is performed on these signals respectively to obtain their IMFs and residuals. The Hilbert transform is performed on all IMFs to obtain the Hilbert spectrum, and the instantaneous energy curves are obtained according to Eq. (2). The Hilbert transform is a time domain signal processing method, the signal time domain energy commonly characterized by the signal envelope which obtained by the Hilbert transform. The comparison of time domain energy and instantaneous energy is shown in Fig. 7. The red dotted boxes mark the energy curves of the non-direct wave portion. It can be seen that the instantaneous energy curve is more concentrated at the direct wave and the energy difference is more obvious, which has a better performance for characterizing the damage.

An effective time window was set with the peak of the instantaneous energy curve as the center, and the length was about the length of the excitation signal period. The portion of the signal that is directly affected by the damage can be extracted which could reduce the influence of boundary reflections on the damage feature extraction. In this paper, the effective time window was set to 40 μ s. The EVDI and

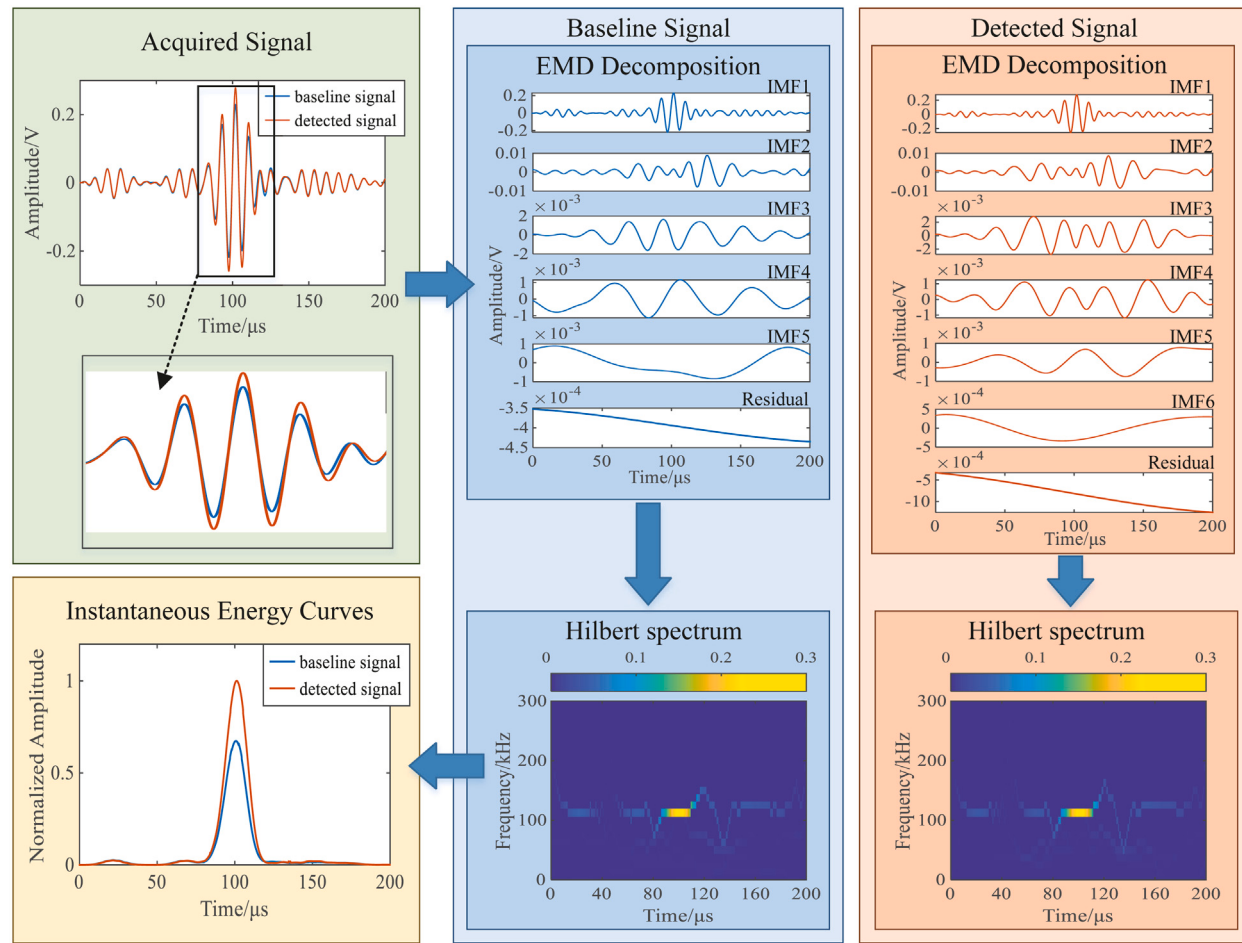


Fig. 6. Signal processing process of UGW acquired from sensor path P_{1-8} .

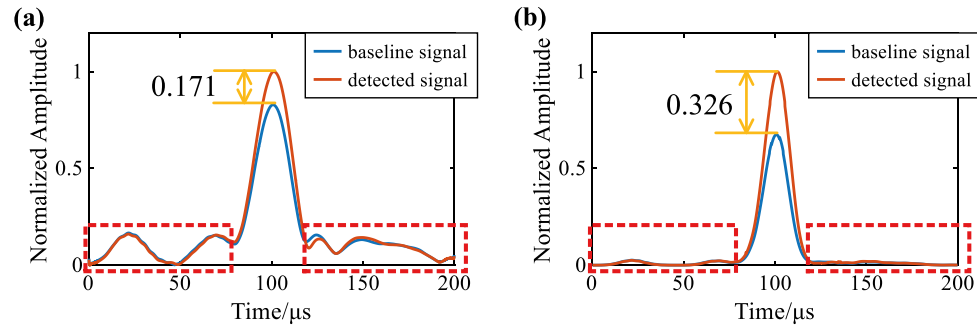


Fig. 7. The comparison of time domain energy and instantaneous energy (a) time domain energy curve, (b) instantaneous energy curve.

ERDI calculated with the curves within the time window are shown in Fig. 8.

In Fig. 8, the sensor paths that are directly through the damage are marked in purple and the paths near them are marked in red. It can be seen that the DI of the path directly through the damage is not the largest and is always less or approximated to the damage index of the paths adjacent to them (this phenomenon appears in all 74 tested experiments). However, the probability distribution function in the probabilistic imaging algorithm obeys the principle that the weight value decreases gradually from the point on the path to both sides. The mismatch between the distribution phenomenon of the DI and the distribution pattern of the weights will lead to a large error in the imaging results [36,37].

The instantaneous energy curves of P_{1-6} , P_{1-7} , and P_{1-8} are shown in Fig. 9 in order, where P_{1-7} is the sensor path that directly through the damage, and P_{1-6} and P_{1-8} are sensor paths near the damage. The interaction between the UGW and the damage mainly shows the behavior of transmission and scattering, which results in the response signal changes. When the sensor path passes directly through the damage, the direct wave is attenuated and generates scattered waves in other directions due to the blockage of the damage, resulting in an energy decrease. When the sensor path has a certain distance from the damage, the direct wave will be received completely and a part of the scattered wave will be superimposed into the direct wave, resulting in an energy increase. As the distance increases, the scattered wave that can be superimposed gradually become less, and eventually the damage will not affect the direct waves.

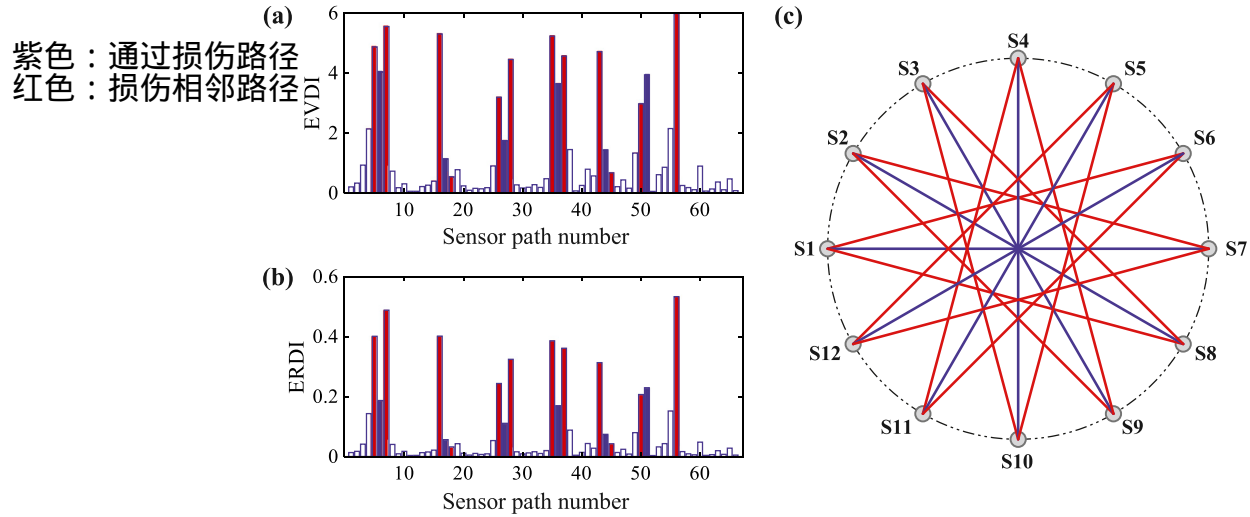


Fig. 8. Damage index based on instantaneous energy (a) EVDI, (b) ERDI, (c) sensor path location.

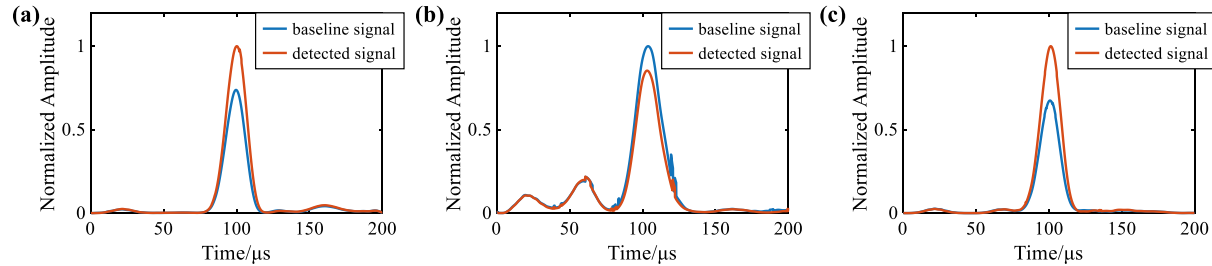
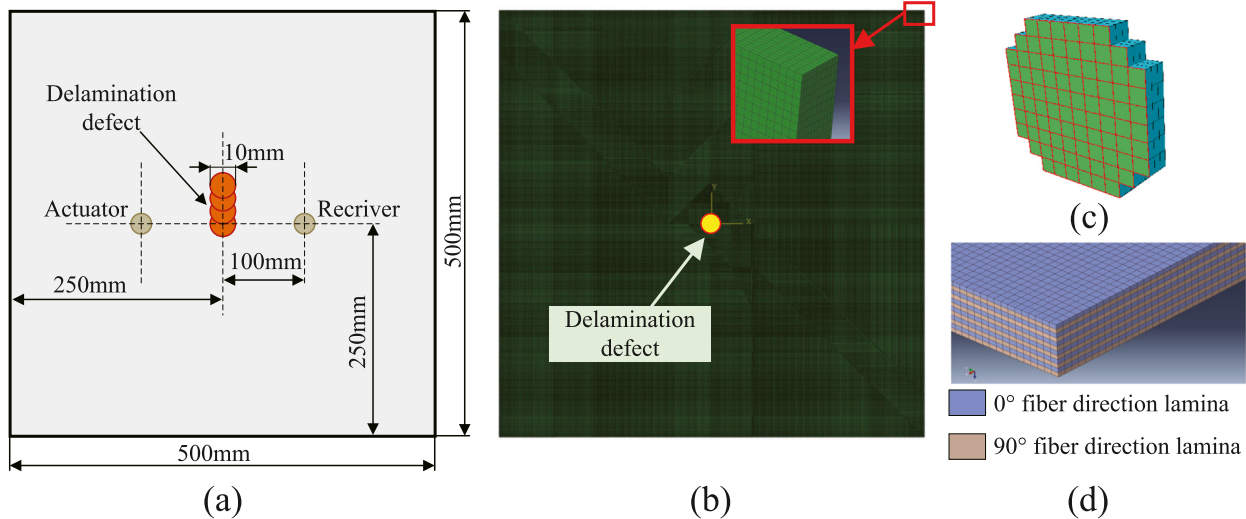
Fig. 9. Instantaneous energy curve (a) sensor path P_{1-6} , (b) sensor path P_{1-7} , (c) sensor path P_{1-8} .

Fig. 10. Numerical simulation setup (a) schematic diagram, (b) finite element model, (c) the set of failed elements representing geometry of delamination defect, (d) material orientation.

3.5. Numerical simulation

The numerical simulation experimental setup is shown in Fig. 10. The simulation model of the carbon fiber composite plate used is built by the ABAQUS finite element simulation software. The modeled material parameters are shown in Table 3. The composite layer connection is simulated by using 0 thickness cells between the third and fourth layers. Delamination defects are simulated by cell failure. Four circular delamination defects of 10 mm diameter with the distance from the

center to the sensor path of 0 mm, 5 mm, 10 mm, and 15 mm were set up.

The response signals and instantaneous energy curves are shown in Figs. 11 and 12, respectively. Where the energy decrease occurs at 0 mm and 5 mm, the energy increase occurs at 10 mm, when the distance increases to 15 mm, the energy curve is basically unchanged. The UGW propagation in the plate is shown in Fig. 13, where the red circle is the sensor and the orange circle is the delamination defect. The color scale represents the UGW amplitude. The increase or decrease in

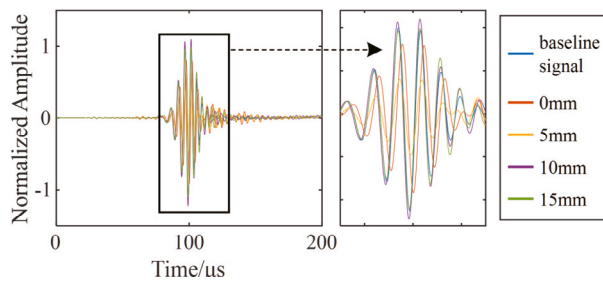


Fig. 11. Receiving signals of numerical simulation.

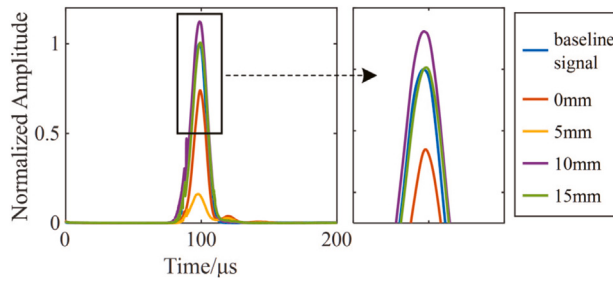


Fig. 12. Instantaneous energy curve of receiving signals.

UGW amplitude occurs at the receiver due to the damage. In Fig. 13(b), the receiver acquires the direct wave affected by the damage, which occurs energy decrease. In Fig. 13(c), the low amplitude UGW appears at the receiver, which occurs a large energy decrease. In Fig. 13(d), the scattered signal and the direct wave are superimposed at the receiver, and an energy increase occurs. In Fig. 13(e), the scattered signal can no longer be superimposed in the direct wave due to the large propagation distance, so basically no energy change occurs. The results show that the difference of instantaneous energy can be an effective way to quantify the damage information, but only considering the absolute amount of change without considering the increase or decrease may cause that the damage far from the sensor path is able to make the sensor path a large DI, thus affecting the localization results.

结果表明，应关注能量的增减

4. Method improvement and result discussion

4.1. Method improvement

Eqs. (6) and (7) are modified to Eqs. (8) and (9), respectively, as follows:

$$EVDI = \int |\widetilde{IE}_x(t) - \widetilde{IE}_y(t)| dt, \quad (8)$$

$$ERDI = \int \frac{|IE_x(t) - IE_y(t)|}{IE_x(t)} dt. \quad (9)$$

The absolute value of DI represents the quantization result of damage, and the sign indicates the property of energy increase or decrease. When the energy of the detection signal is less than the energy of the baseline signal, the result is plus, which means that energy decrease; conversely, the result is minus, which means that energy increase.

According to Section 3, for the same side of a sensor path, the damage that causes energy increase is always farther from the sensor path than the damage that causes energy decrease. Therefore a probability distribution function based on the elliptical method has been introduced, in which maximum weight is on the ellipse with the sensor as the focus and decreases to both sides. The function is expressed as:

$$EW_k[R_k(x, y)] = \begin{cases} 1 - \left[\frac{R_k(x, y)}{\beta} - 1 \right], & \beta \leq R_k(x, y) < 2\beta \\ 1 + \left[\frac{R_k(x, y)}{\beta} - 1 \right], & R_k(x, y) < \beta \end{cases}. \quad (10)$$

When the energy decrease occurs, the sensor path is through the damage, and the traditional probability distribution function is selected. When the energy increase occurs, the sensor path is near the damage, and the probability distribution function based on the elliptical method is selected. At this point, Eq. (3) will be modified to Eq. (11) as follow:

$$P(x, y) = \sum_{k=1}^N p_k(x, y) = \sum_{i=1}^I |DI_i| TW_i[R_i(x, y)] + \sum_{j=1}^J |DI_j| EW_j[R_j(x, y)], \quad (11)$$

能量减少：
传统计算法

where I is the number of paths through the damage and J is the number of paths near the damage.

In summary, Fig. 14 is a flow chart of the proposed method and the steps are specified as follows:

(1) DI extraction: HHT is performed on the baseline signal and the detection signal to obtain the instantaneous energy curve. The DI with energy increase and decrease property based on the instantaneous energy characteristic is extracted.

(2) Path classification: The sensor path classification based on energy increase and decrease property is performed to determine the choice of probability distribution function.

(3) Damage imaging: The damage diagnosis image and localization coordinates are obtained by a probabilistic imaging algorithm.

4.2. Result discussion

The experimental data of the test point (0, 0) in Section 3 was reprocessed, and the modified EVDI and ERDI were obtained as shown in Fig. 15. In both DI calculations the red bars indicating adjacent paths are in the negative half of the bar charts, while the purple bars indicating direct paths are in the positive half.

Using EVDI and ERDI respectively, the imaging results of the traditional probabilistic imaging method, the probabilistic imaging method based on the elliptical method, and the proposed improved method are shown in Fig. 16. The color in the figure indicates the normalized damage probability, and the coordinates of the pixel point with the maximum value are selected as the localization result. The improved method obtained the localization coordinates as (-5.2, 0.1), (-4.5, 2.7) by using EVDI and ERDI, respectively. However, the coordinates obtained by the traditional probabilistic imaging method are (19.7, -5.6), (21.7, -17.7), and the probabilistic imaging method based on the elliptical method is (-5.2, 1.1), (-4.1, 4.1).

The remained test points data are processed. Here the time domain energy curves obtained using the HT method are used for comparison. The DIs obtained using Eqs. (6) and (8), Eqs. (7) and (9) are denoted as HT-EVDI and HT-ERDI, respectively. Otherwise, the signal difference coefficient (SDC), a damage characterization method based on the Pearson coefficient, is one of the most commonly used damage indices in traditional probabilistic imaging method and more sensitive to the phase deviation [38,39]. It was joined in the comparative analysis.

Due to the average localization errors obtained by the probabilistic imaging method based on the elliptical method with EVDI, ERDI, HT-EVDI, and HT-ERDI respectively are 29.43 mm, 26.49 mm, 27.92 mm, and 27.84 mm, which much higher than the other two imaging methods. Therefore, the main comparison between the traditional probabilistic imaging method and the improved method follows. In Fig. 17, the distribution of the localization error is plotted in the fourth quadrant. The higher luminance indicates the larger localization error at that test point, and when the localization error is greater than 10 mm, the maximum luminance is given. The Localization errors are summarized in Fig. 18.

For all four DIs, the localization results obtained by the improved method were better than those with traditional method. SDC has the best localization performance in the traditional method, but is weaker than the localization effect of each damage index in the improved

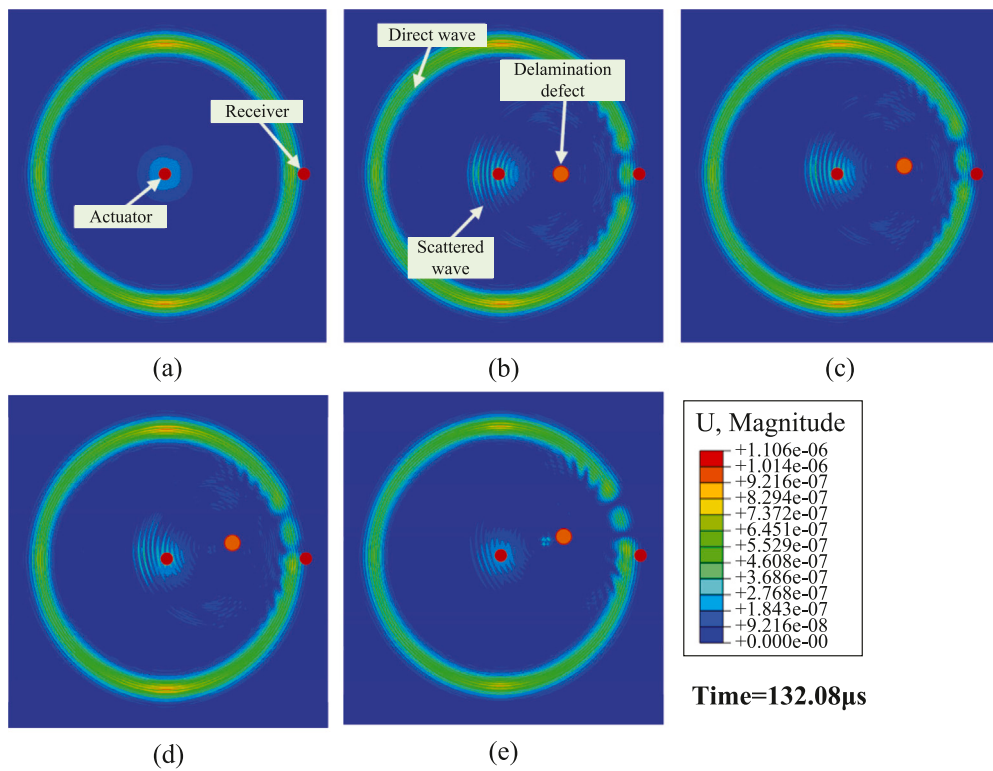


Fig. 13. Propagation of UGWs in the composite plate (a) initial plate, (b) 0 mm, (c) 5 mm, (d) 10 mm, (e) 15 mm.

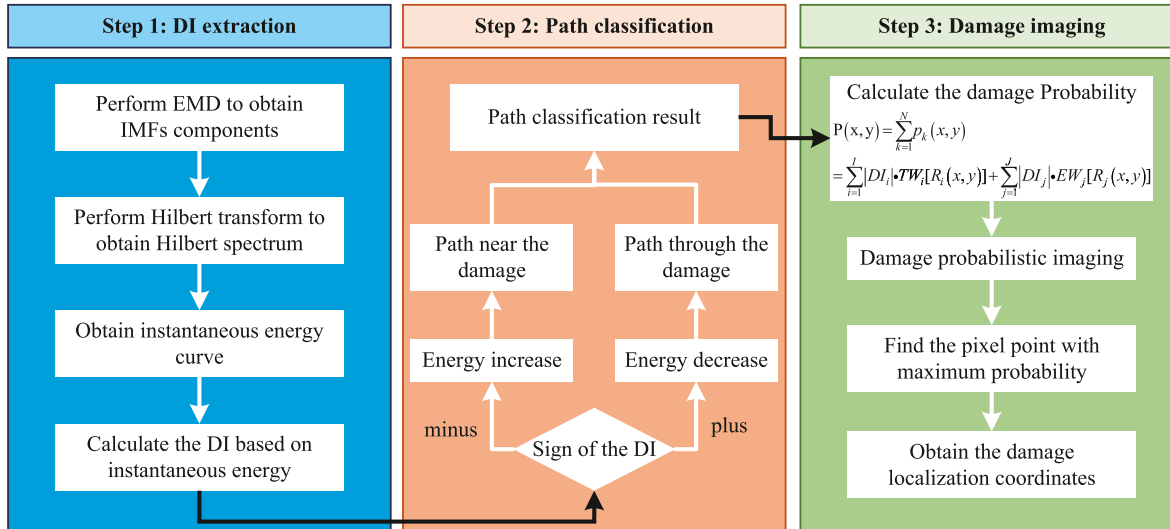


Fig. 14. Flow chart of the proposed method.

method. For the improved method, when the same DI formula is used, the effect of the instantaneous energy obtained by HHT is better than that of the time domain energy obtained by HT. The improved method with *ERDI* has the best localization results among all methods. Note, among the 74 test points in this paper, improved method with *ERDI* is the only method that does not appear to locate the test point on the proximity sensor. This indicates that this method has a certain suppression effect on the detection blindness phenomenon due to proximity to the sensor in the traditional probabilistic imaging method. Therefore, *ERDI* is selected as the DI of the proposed improved method in this paper. The localization results of all 74 test points obtained by the proposed improved method with *ERDI* are shown in Table 4. The average error is 3.56 mm, the maximum error does not exceed 10 mm,

and 75.68% of the localization errors are within 5 mm, which are better than the comparison methods in all indexes.

5. Conclusion

This article studied the UGW damage imaging method and its application in a carbon fiber composite plate. The study results are summarized as follows.

(1) Proposed a probabilistic imaging damage localization method based on UGW instantaneous energy characteristics. The traditional probabilistic imaging method is improved by introducing a probability distribution function based on the elliptical method. According to the rule of signal instantaneous energy increase or decrease property and

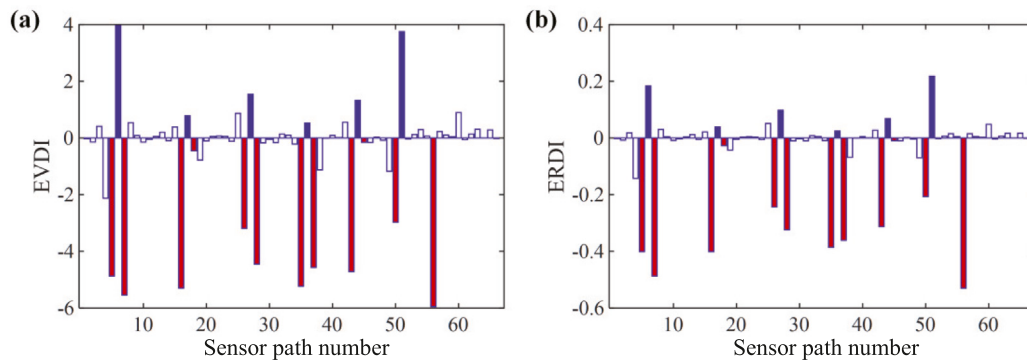


Fig. 15. Modified damage index (a) EVDI, (b) ERDI.

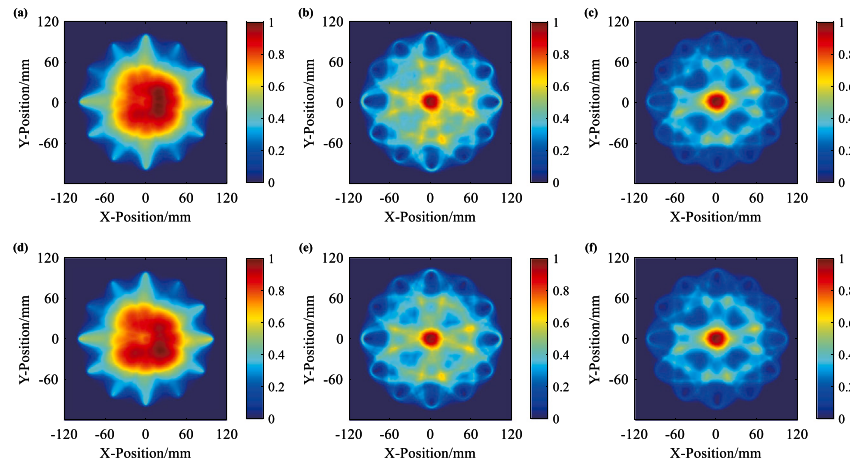


Fig. 16. The imaging results at point (0, 0) (a) and (d) are the traditional probabilistic imaging method with EVDI and ERDI; (b) and (e) are the probabilistic imaging method based on the elliptical method with EVDI and ERDI; (c) and (f) are the improved method with EVDI and ERDI.

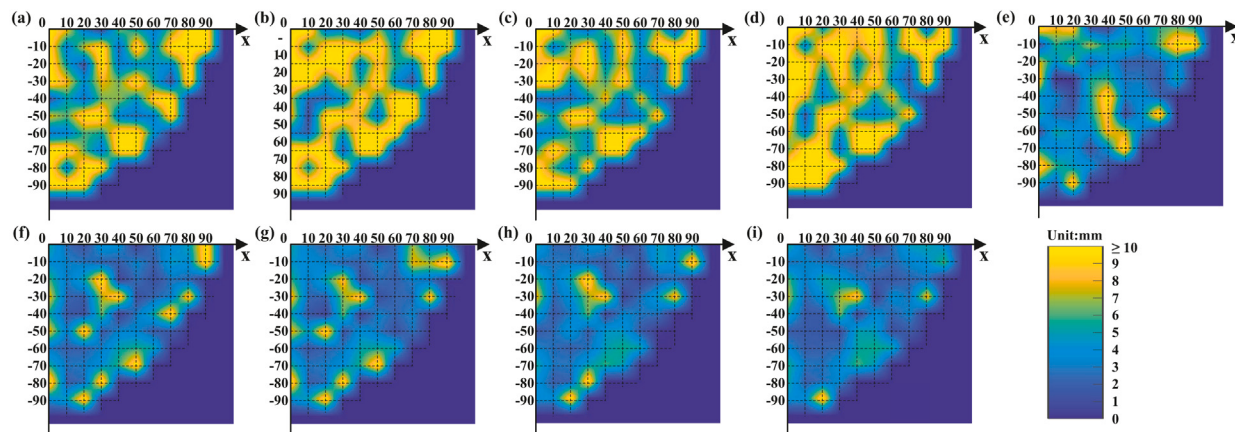


Fig. 17. Localization error at the fourth quadrant (a) (b) (c) (d) and (e) are the traditional method with HT-EVDI, HT-ERDI, EVDI, ERDI and SDC; (f) (g) (h) and (i) are the improved method with HT-EVDI, HT-ERDI, EVDI and ERDI.

distance from damage to sensor path, the sensor paths are classified to apply different probability distribution functions. The damage imaging results of the improved method are imaged by fusing the paths using the traditional probability distribution function and the paths using the elliptical method probability distribution function.

(2) The proposed method has highly accurate and stable damage localization results. Experiments were performed on a carbon fiber composite plate. Experimental results show that the ERDI has better damage characterization capability. The absolute error of the pro-

posed method is less than 10 mm, the average error is 3.56 mm, and the standard deviation of the error is 1.99 mm. Furthermore, the proposed method has a suppression effect on the detection blindness phenomenon in the traditional probabilistic imaging method.

This research can apply to the development of online health monitoring systems for composite plate structures of high-end equipment. In the follow-up research, the relationship between instantaneous energy characteristics and damage size will be further studied for quantitative identification of damage.

Table 4

Localization results by the proposed improved method with ERDI (unit: mm).

Damage coordinate	Localization coordinate	Absolute error	Damage coordinate	Localization coordinate	Absolute error	Damage coordinate	Localization coordinate	Absolute error
(0,0)	(-4.5,2.7)	5.247	(50,-20)	(51.7,-20.2)	1.711	(40,-50)	(38.8,-54.8)	4.948
(10,0)	(9.5,2.5)	2.549	(60,-20)	(60,-18.5)	1.5	(50,-50)	(48.4,-54.3)	4.588
(20,0)	(20.5,-0.9)	1.029	(70,-20)	(69.6,-22.1)	2.138	(60,-50)	(60.1,-51.1)	1.104
(30,0)	(26,0)	4	(80,-20)	(77.5,-19.6)	2.532	(70,-50)	(68.5,-49.1)	1.749
(40,0)	(36.4,0)	3.6	(0,-30)	(-1.2,-37)	7.102	(0,-60)	(0,-56.6)	3.4
(50,0)	(50.3,-0.5)	0.583	(10,-30)	(8.5,-31.7)	2.267	(10,-60)	(10.3,-61.8)	1.825
(60,0)	(57.6,-0.8)	2.53	(20,-30)	(22.8,-27.2)	3.959	(20,-60)	(18,-60.4)	2.039
(70,0)	(70.6,-4.6)	4.638	(30,-30)	(23.6,-27.8)	6.767	(30,-60)	(28.8,-62)	2.332
(80,0)	(84.3,-2.4)	4.924	(40,-30)	(30.9,-27.4)	9.464	(40,-60)	(37,-64.2)	5.161
(90,0)	(86,-0.2)	4.005	(50,-30)	(49.7,-30.2)	0.36	(50,-60)	(53,-64.7)	5.575
(0,-10)	(-2.5,-9.7)	2.517	(60,-30)	(63.4,-31.4)	3.677	(60,-60)	(56.2,-56.6)	5.1
(10,-10)	(12.7,-8.3)	3.19	(70,-30)	(72.6,-30.8)	2.72	(0,-70)	(-5.4,-69.2)	5.459
(20,-10)	(18.6,-12.5)	2.865	(80,-30)	(71.1,-32.1)	9.144	(10,-70)	(9.3,-67.3)	2.789
(30,-10)	(31.7,-8.5)	2.267	(0,-40)	(-5,-39.3)	5.048	(20,-70)	(22.5,-69.3)	2.596
(40,-10)	(40.5,-8.4)	1.676	(10,-40)	(8.5,-40.6)	1.615	(30,-70)	(30.4,-73.8)	3.821
(50,-10)	(46.9,-11.2)	3.324	(20,-40)	(21.3,-41.1)	1.703	(40,-70)	(34.1,-70)	5.9
(60,-10)	(61,-12.1)	2.325	(30,-40)	(24.7,-43.8)	6.521	(50,-70)	(45.5,-71.3)	4.684
(70,-10)	(66.7,-10.1)	3.301	(40,-40)	(40.2,-40.7)	0.728	(0,-80)	(-1.5,-75.1)	5.124
(80,-10)	(80.1,-14)	4.001	(50,-40)	(46.4,-41.6)	3.939	(10,-80)	(11.3,-81.3)	1.838
(90,-10)	(84.1,-10.9)	5.968	(60,-40)	(57.8,-39.9)	2.202	(20,-80)	(19.6,-77.5)	2.531
(0,-20)	(0,-26)	6	(70,-40)	(69.3,-36.8)	3.276	(30,-80)	(28.4,-76.9)	3.489
(10,-20)	(12.5,-18.6)	2.865	(0,-50)	(0,-51.7)	1.7	(0,-90)	(-0.1,-86)	4.001
(20,-20)	(20.4,-25.2)	5.215	(10,-50)	(10.2,-48.3)	1.712	(10,-90)	(6.6,-88.3)	3.801
(30,-20)	(25.9,-21.8)	4.477	(20,-50)	(18.5,-49.8)	1.513	(20,-90)	(14.4,-82.1)	9.683
(40,-20)	(41.9,-22.3)	2.983	(30,-50)	(31.2,-50)	1.2			

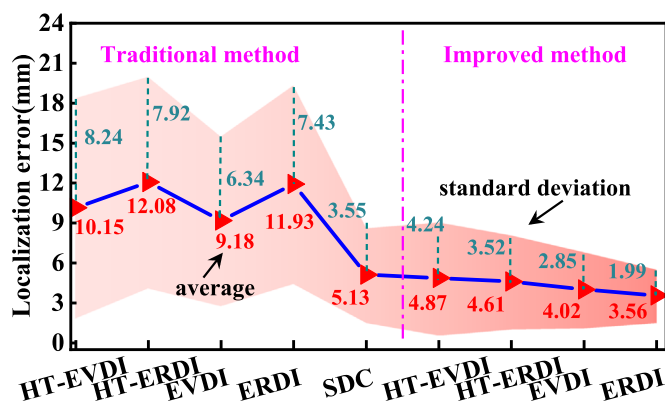


Fig. 18. The summary of Localization error.

CRediT authorship contribution statement

Feiyu Teng: Conceptualization, Data curation, Formal analysis, Investigation, Methodology, Validation, Writing – original draft, Writing – review & editing. **Juntao Wei:** Data curation, Investigation, Supervision, Validation. **Shanshan Lv:** Conceptualization, Methodology, Writing – review & editing. **Xiangyi Geng:** Conceptualization, Formal analysis, Writing – review & editing. **Chang Peng:** Conceptualization, Investigation, Formal analysis. **Lei Zhang:** Data curation, Software, Validation. **Zengye Ju:** Supervision, Investigation, Formal analysis. **Lei Jia:** Conceptualization, Funding acquisition, Resources. **Mingshu Jiang:** Methodology, Funding acquisition, Project administration, Resources, Supervision, Writing – review & editing.

Declaration of competing interest

The authors declare that they have no known competing financial interests or personal relationships that could have appeared to influence the work reported in this paper.

Data availability

The data that has been used is confidential.

Acknowledgments

This work was supported by National Key Research and Development Project of China [grant number 2020YFE0204900]; National Natural Science Foundation of China [grant numbers 62073193, 61903224]; and Key research and development plan of Shandong Province [grant number 2021CXGC010204].

References

- [1] W. Nsengiyumva, S. Zhong, J. Lin, et al., Advances, limitations and prospects of nondestructive testing and evaluation of thick composites and sandwich structures: A state-of-the-art review, Compos. Struct. 256 (2021) 112951.
- [2] A. Stawiarski, The nondestructive evaluation of the GFRP composite plate with an elliptical hole under fatigue loading conditions, Mech. Syst. Signal Process. 112 (2018) 31–43.
- [3] H. Rocha, C. Semprinoschnig, J.P. Nunes, Sensors for process and structural health monitoring of aerospace composites: A review, Eng. Struct. 237 (2021) 112231.
- [4] J. Zhang, D. Yao, R. Wang, et al., Vibro-acoustic modelling of high-speed train composite floor and contribution analysis of its constituent materials, Compos. Struct. 256 (2021) 113049.
- [5] L. Huang, L. Zeng, J. Lin, et al., An improved time reversal method for diagnostics of composite plates using lamb waves, Compos. Struct. 190 (2018) 10–19.
- [6] Y. Ren, L. Qiu, S. Yuan, et al., Gaussian mixture model and delay-and-sum based 4D imaging of damage in aircraft composite structures under time-varying conditions, Mech. Syst. Signal Process. 135 (2020) 106390.
- [7] S. Gholizadeh, A review of non-destructive testing methods of composite materials, Procedia Struct. Integr. 1 (2016) 50–57.
- [8] P. Duchene, S. Chaki, A. Ayadi, et al., A review of non-destructive techniques used for mechanical damage assessment in polymer composites, J. Mater. Sci. 53 (2018) 7915–7938.
- [9] V. Memmolo, E. Monaco, N.D. Boffa, et al., Guided wave propagation and scattering for structural health monitoring of stiffened composites, Compos. Struct. 184 (2018) 568–580.
- [10] R. Cui, C. Wiggers de Souza, B.J. Katko, et al., Non-destructive damage localization in built-up composite aerospace structures by ultrasonic guided-wave multiple-output scanning, Compos. Struct. 292 (2022) 115670.
- [11] J.Y.H. Chu, C.R.P. Courtney, The detection of impact damage to the edges of CFRP plates using extensional ultrasonic edge waves, J. Nondestruct. Eval. 40 (2021) 88.
- [12] R. Gorgin, Y. Luo, Z. Wu, Environmental and operational conditions effects on lamb wave based structural health monitoring systems: A review, Ultrasonics 105 (2020) 106114.

- [13] H. Chen, X. Nie, S. Gan, et al., Interfacial imperfection detection for steel-concrete composite structures using NDT techniques: A state-of-the-art review, *Eng. Struct.* 245 (2021) 112778.
- [14] R. Soleimani, C. Ng, Locating delaminations in laminated composite beams using nonlinear guided waves, *Eng. Struct.* 131 (2017) 207–219.
- [15] S. He, C. Ng, A probabilistic approach for quantitative identification of multiple delaminations in laminated composite beams using guided waves, *Eng. Struct.* 127 (2016) 602–614.
- [16] M.V. Burkov, A.V. Eremin, A.V. Byakov, et al., Impact damage detection in laminate and honeycomb CFRPs using lamb wave ultrasonic sensing, *Russ. J. Nondestruct. Test.* 57 (2021) 114–124.
- [17] J. Wang, T. Wang, Q. Luo, A practical structural health monitoring system for high-speed train car-body, *IEEE Access* 7 (2019) 168316–168326.
- [18] D. Wang, L. Ye, Z. Su, et al., Probabilistic damage identification based on correlation analysis using guided wave signals in aluminum plates, *Struct. Health Monit.* 9 (2) (2010) 133–144.
- [19] N. Yue, Z.S. Khodaei, M.H. Aliabadi, Damage detection in large composite stiffened panels based on a novel SHM building block philosophy, *Smart Mater. Struct.* 30 (2021) 045004.
- [20] B. Feng, D.J. Pasadas, A.L. Ribeiro, et al., Locating defects in anisotropic CFRP plates using tof-based probability matrix and neural networks, *IEEE Trans. Instrum. Meas.* 68 (2019) 1252–1260.
- [21] J. Lin, F. Gao, Z. Luo, et al., High-resolution lamb wave inspection in viscoelastic composite laminates, *IEEE Trans. Ind. Electron.* 63 (2016) 6989–6998.
- [22] A. Akan, O. Karabiber Cura, Time-frequency signal processing: Today and future, *Digit. Signal Process.* 119 (2021) 103216.
- [23] M.S. Hameed, Z. Li, K. Zheng, Damage detection method based on continuous wavelet transformation of lamb wave signals, *Appl. Sci.* 10 (2020) 8610.
- [24] Y. Lu, J. Tang, On time-frequency domain feature extraction of wave signals for structural health monitoring, *Measurement* 114 (2018) 51–59.
- [25] N.E. Huang, Z. Shen, S.R. Long, et al., The empirical mode decomposition and the Hilbert spectrum for nonlinear and non-stationary time series analysis, *Proc. R. Soc. Lond. Ser. A* 454 (1998) 903–995.
- [26] M. Liu, J. Yang, Y. Cao, et al., A new method for arrival time determination of impact signal based on HHT and AIC, *Mech. Syst. Signal Process.* 86 (2017) 177–187.
- [27] A. Soualhi, K. Medjaher, N. Zerhouni, Bearing health monitoring based on Hilbert-Huang transform, support vector machine, and regression, *IEEE Trans. Instrum. Meas.* 64 (2015) 52–62.
- [28] L.-S. Law, J.H. Kim, W.Y.H. Liew, et al., An approach based on wavelet packet decomposition and Hilbert–Huang transform (WPD–HHT) for spindle bearings condition monitoring, *Mech. Syst. Signal Process.* 33 (2012) 197–211.
- [29] L. Lin, F. Chu, HHT-based AE characteristics of natural fatigue cracks in rotating shafts, *Mech. Syst. Signal Process.* 26 (2012) 181–189.
- [30] B.C. Xu, M.L. Wang, Q. Jia, Application of marginal spectrum in active lamb wave damage monitoring of plate structure, *Appl. Mech. Mater.* 490–491 (2014) 1698–1701.
- [31] B. Xu, M. Wang, P. Li, et al., Application of instantaneous parameter characteristic in active lamb wave based monitoring of plate structural health, *Appl. Sci.* 10 (2020) 5664.
- [32] C. Su, M. Jiang, J. Liang, et al., Damage identification in composites based on Hilbert energy spectrum and lamb wave tomography algorithm, *IEEE Sens. J.* 19 (2019) 11562–11572.
- [33] M. Barski, A. Stawiarski, The crack detection and evaluation by elastic wave propagation in open hole structures for aerospace application, *Aerosp. Sci. Technol.* 81 (2018) 141–156.
- [34] F. Gao, Y. Shao, J. Hua, et al., Enhanced wavefield imaging method for impact damage detection in composite laminates via laser-generated lamb waves, *Measurement* 173 (2021) 108639.
- [35] B. Wang, W. Shi, B. Zhao, et al., A modal decomposition imaging algorithm for ultrasonic detection of delamination defects in carbon fiber composite plates using air-coupled lamb waves, *Measurement* 195 (2022) 111165.
- [36] G. Liu, Y. Xiao, H. Zhang, G. Ren, et al., Probability-based diagnostic imaging for damage identification of stiffened composite panel, *Acta Mater. Compos. Sin.* 35 (2) (2018) 311–319.
- [37] G. Azuara, E. Barrera, M. Ruiz, et al., Damage detection and characterization in composites using a geometric modification of the RAPID algorithm, *IEEE Sens. J.* 4 (2020) 2084–2093.
- [38] F. Teng, J. Wei, S. Lv, et al., Ultrasonic guided wave damage localization in hole-structural bearing crossbeam based on improved RAPID algorithm, *IEEE Trans. Instrum. Meas.* 71 (2022) 3524513.
- [39] A. Gonzalez-Jimenez, L. Lomazzi, F. Cadini, et al., On the mitigation of the RAPID algorithm uneven sensing network issue employing averaging and Gaussian blur filtering techniques, *Compos. Struct.* 278 (2021) 114716.